

1 Deep and rapid thermo-mechanical erosion by a
2 small-volume lava flow

3 Gallant, E.¹ (egallant@mail.usf.edu), Deng, F.¹, Connor, C.¹,
Dixon, T.H.¹, Xie, S.¹, Saballos, J.A.², Guitierrez, C.²,
Myhre, D.³, Connor, L.¹, Zayac, J.⁴, LaFemina, P.⁵, Charbonnier,
S.¹, Richardson, J.^{6,7}, Maslervisi, R.¹, and Thompson, G.¹

- 1: University of South Florida, School of Geosciences
2: Instituto Nicaragüense de Estudios Territoriales
3: University of South Florida, College of Marine Science
4: Queens College, Department of Earth and Environmental Sciences
5: Pennsylvania State University, Department of Geosciences
6: NASA Goddard Space Flight Center
7: University of Maryland, Department of Astronomy

4 October 7, 2019

5 **Abstract**

6 We document remarkably efficient thermo-mechanical erosion by a small-
7 volume lava flow. Downcutting by a basaltic-andesite lava flow on the
8 steep-sided Momotombo volcano, Nicaragua, occurred at 100 times the
9 rate commonly reported for thermal erosion in lava flow fields, even though
10 this flow was small-volume (0.02 km³) and effused at a low rate for <1
11 week. The erosion depth, up to 30 m incision, is explained by reduction of
12 hardness, H , of the pyroclastic substrate into which the lava flow incised.
13 We show that incision depth decreases, approximately exponentially, with
14 distance along the flow path, until erosion stopped and the flow became
15 constructional. This transition occurs 650 m from the vent on a slope
16 averaging a 32° incline. Results indicate that syn-eruptive erosion is an
17 important morphological process on some steep-sided volcanoes that are
18 predominantly composed of layered pyroclasts. Rapid erosion and incision
19 increased flow run-out for the 1905 flow, which in turn directed the flow
20 and run-out of the 2015 lava flow. Mapping and understanding these fea-
21 tures is critical for improving lava flow hazard assessments and provides
22 insight into the construction and growth of composite cones.

23
24 **Keywords:** lava flow physics; thermal and mechanical erosion; lava in-
25 undation; volcano morphology; remote sensing; thermal dynamics of lava
26 flows

27 **1 Introduction**

28 Lava flows are responsible for altering landscapes on geologically short timescales.
29 The overwhelming majority of lava flows construct topography by building
30 raised channels and/or compound flow fields, both of which evolve through
31 time and along-flow (Kerr et al., 2006; Dietterich and Cashman, 2014). The
32 morphologies of flow features are mainly determined by the composition and ef-
33 fusion rate of the flow, as well as the pre-existing and syn-eruptive topography
34 (Richardson and Karlstrom, 2019; Bilotta et al., 2019). These factors also con-
35 trol the thickness of lava flows, which in turn influence a flow’s run-out distance
36 and inundation hazard potential (Kilburn and Lopes, 1988; Dietterich et al.,
37 2017). A small fraction of channelized flows and lava tubes erode into older
38 surfaces during emplacement via thermal, mechanical, or thermo-mechanical
39 processes (Greeley et al., 1998; Fagents and Greeley, 2001; Kerr, 2001; Siewert
40 and Ferlito, 2008; Hurwitz et al., 2010, 2013).

41 The 1905 eruption of Momotombo volcano, Nicaragua, provides an exam-
42 ple of thermo-mechanical erosion by a small volume ($<0.02 \text{ km}^3$) lava flow on
43 a steep-sided edifice (Figs. 1 and 2). We first document the morphology of
44 the channel using a combination of satellite and terrestrial radar generated dig-
45 ital elevation models (DEMs) from 2012–2017. Erosion depths from the 1905
46 flow are then calculated by reconstructing pre-channel topography, extracting
47 cross-sectional profiles, and calculating the maximum difference between the
48 measured and modeled surfaces normal to the channel. We use these results
49 to test thermal and thermo-mechanical models of erosion. Model inputs are in-
50 formed by observations from Momotombo’s most recent eruption in 2015, which
51 we capture with the range of our satellite observations. We find the channel was
52 thermo-mechanically eroded by a lava flow that erupted in 1905. Additionally,
53 we assert that thermo-mechanical erosion is an important morphological process

54 on some steep-sided volcanoes composed predominantly of layered pyroclasts.
55 This study is the first to look at lava flow erosion on steep sided slopes, expands
56 our knowledge of the rate at which syn-eruptive erosion occurs, and mathemat-
57 ically couples thermal and mechanical models of erosion.

58 **2 Background**

59 **2.1 Erosion by Lavas**

60 Erosion by lava has been hypothesized for the formation of rilles on both Mars
61 (Dundas and Keszthelyi, 2014) and the Moon (Head and Wilson, 2017; Wilson
62 and Head, 2017), canali on Venus (Baker et al., 1992; Williams-Jones et al.,
63 1998), and channels on Io (Schenk and Williams, 2004). Studies of active erosion
64 by flowing lava have occurred on the island of Hawai'i during the 1972–1974
65 Mauna Ulu eruption and the initial stages of the 1983-2018 Pu'u O'o eruption,
66 where erosion rates of 4 cm depth/day and 10 cm depth/day were observed in
67 lava tubes via skylights, respectively (Peterson et al., 1994; Kauahikaua et al.,
68 1998). Erosion by turbulent komattite flows during the Archean, responsible
69 for large Ni-sulphide ore deposits, is also widely noted (Williams et al., 1998;
70 Beresford et al., 2002; Staude et al., 2017).

71 **Thermal Erosion**

72 Thermal erosion occurs when lava moves with sufficient flux and temperature to
73 melt and incise the underlying terrain (Kerr, 2001). Thermal erosion by flowing
74 lava requires the complete or partial melting and assimilation of a substrate
75 into the overriding flow. A lava flow's total available thermal energy ($E_{thermal}$),
76 sourced from advection and crystallization, is modeled as:

$$E_{thermal} = m_l[c_{pl}(T_l - T_a) + \phi F] \quad (1)$$

77 where m_l is the mass of the erupted lava, c_{pl} is the specific heat capacity of
 78 the lava, T_l is the erupted temperature of the lava, T_a is the temperature of the
 79 environment into which heat is being transferred (the substrate in this case), ϕ
 80 is the mass fraction crystallization, and F is the latent heat of fusion (Wooster
 81 et al., 1997). Lava flows are an open system where available thermal energy
 82 is eventually balanced out by heat loss through conduction, convection, and
 83 radiative heat transfer. Studies of the thermal energy balance of lava flows on
 84 Mt Etna show that upwards of 85% of energy was retained during the initial
 85 phases of the eruption, which can be used to further bound the amount of energy
 86 available to melt and erode the substrate (Wooster et al., 1997; Patrick et al.,
 87 2004). The presence of multiple heat sinks also highlights the fact that not all
 88 available thermal energy can be partitioned into eroding the substrate, so we
 89 need to quantify heat transfer between the base of the lava flow and substrate.
 90 The rate of conductive heat transfer into the substrate (i.e., the growth of a
 91 thermal boundary layer) can be modeled as:

$$\frac{dy}{dt} = \frac{\eta_T \sqrt{\kappa}}{t} \quad (2)$$

92 where y is the depth into the substrate, t is the duration of the flow, and η_T is
 93 a dimensionless similarity variable (Turcotte et al., 2002; Fagents and Greeley,
 94 2001). The growth of this boundary layer is illustrated in Figure 3.

95 **Mechanical Erosion**

96 Mechanical erosion occurs when the wearing material (the lava flow) is harder
 97 than the substrate (the edifice) (Sklar and Dietrich, 1998; Siewert and Ferlito,
 98 2008; Hurwitz et al., 2010). The early stages of an eruption are most conducive

99 to erosion because flow velocity is often highest and basal friction is also high due
 100 to the vertical load (Siewert and Ferlito, 2008; Hurwitz et al., 2010). Mechanical
 101 erosion as a function of substrate hardness can be modeled as:

$$H = \frac{k\rho ghv\sin\theta}{d_{channel}} \quad (3)$$

102 where H is the hardness of the substrate, k is a dimensionless proportionality
 103 constant that captures the material hardness of the erosive layer (the lava flow),
 104 ρ is the density of the lava flow, h is the thickness of the lava flow, v is the
 105 velocity of the lava flow, θ is the slope of the edifice, and $d_{channel}$ is the depth
 106 of erosion. This equation implies that the depth of an eroded channel will be
 107 constant, so long as the velocity of the flow is constant. If the depth of the
 108 channel changes with distance, then either the velocity of the flow is changing,
 109 or the hardness, H , is changing, or both.

110 The yield strength is an exponential function of temperature, which means
 111 that H can also be modeled as a function of temperature:

$$H \approx \frac{ae^{(-bT_a)}}{3} \quad (4)$$

112 where a and b are flow-dependent variables that vary with magma composition
 113 and e is Euler's number. This relationship describes softening of the substrate
 114 as temperature increases or for a longer duration of heating, which means that
 115 mechanical lava erosion models presented in Siewert and Ferlito (2008) can be
 116 reworked to become thermo-mechanical models. Values of 1.18×10^5 Pa and
 117 0.12 K^{-1} correspond to a and b for Momotombo. We note that experimental
 118 data have indicated that the Arrhenius relationships shown in Equation 4 break
 119 down around the glass transition point (Miller, 1963; Gottsmann and Dingwell,
 120 2002).

121 **2.2 Geology of Momotombo and Recent Activity**

122 Momotombo (1,297 m) is located at the southern end of the Cordillera de Los
123 Maribios in central Nicaragua (Fig. 1). The edifice is composed primarily of
124 basaltic to basaltic andesite lavas, cinders, and other tephra that erupted dur-
125 ing the last 4,500 years (Kirainov et al., 1988). Sixteen historical eruptions
126 have been documented, the majority of which have been strombolian to violent
127 strombolian (VEI 1-2), with several plinian events (up to VEI 4) (Global Vol-
128 canism Program, 2017). A VEI 4 eruption in 1605-1606 and large earthquake in
129 1610 lead to the abandonment of city of León (Viejo), the capitol of the region
130 at that time (Sapper, 1925). Though the specific morphological changes to the
131 edifice from the 1605-1606 plinian event are not well documented, it's possible
132 that serious damage to the structural integrity of the summit occurred given the
133 impact on surrounding municipalities (Sapper, 1925). The subsequent steady
134 activity throughout the 1800's rebuilt the summit from cinders, agglutinate,
135 and channelized lava flows, as shown in photographs from the late 1800's and
136 early 1900's (Vincent, 1890; Intercontinental Railway Commission, 1898; Sap-
137 per, 1925). Analogous volcanoes, such as Ngauruhoe (New Zealand) (Hobden
138 et al., 2002), Izalco (El Salvador) (Carr and Pontier, 1981), and Cerro Negro
139 (Nicaragua) (Hill et al., 1998; Courtland et al., 2012), have built moderately
140 sized pyroclastic cones in only a few hundred years and can provide insight into
141 the constructional history of Momotombo.

142 The 1905 eruption (VEI 2) occurred between January 16–21 (Sapper, 1925).
143 The basaltic andesite lava flow was accompanied by an eruptive column of suf-
144 ficient height to deposit ash 15 km to the west on the city of León. The effusive
145 component consisted of an eruptive volume of $<0.02 \text{ km}^3$ of basaltic andesite
146 (Fig. 1). Intermittent explosions occurred that sent incandescent blocks and
147 bombs "a great distance" from the crater (Sapper, 1925). First person accounts

148 also describe destruction to the summit during the eruption, which may have
149 resulted in the drainage of a small summit lava lake (Sapper, 1925) (Fig. 2).
150 The 1905 eruption was followed by 110 years of quiescence, which ended on 30
151 November, 2015. A small volume basaltic andesite lava flow was emplaced be-
152 tween 1 December and 7 December, 2015, and was followed by several months
153 of intermittent explosions (Global Volcanism Program, 2017).

154 **3 Methods and Results**

155 **3.1 Digital Elevation Model Generation**

156 **3.1.1 TanDEM-X Satellites**

157 Digital elevation models (DEMs) were generated from TanDEM-X Satellites
158 (TDX) and collected on 24 October, 2012 and 18 March, 2017. These DEMs,
159 which also capture the change in topography due to the eruption in 2015–2016,
160 allow us to obtain baseline measurements for the 1905 channel (Fig. 4) and
161 determine if any erosion occurred during the most recent eruption. The bistatic
162 mode of TDX allows these two satellites to fly in tandem formation and observe
163 the same ground point simultaneously (Krieger et al., 2007). We note that the
164 flight paths for these acquisitions were not the same, which resulted in an offset
165 due to a heading difference of $\sim 21^\circ$.

166 GAMMA software was used to process the TDX SAR images to generate
167 DEMs with the InSAR (Interferometric Synthetic Aperture Radar) technique
168 (e.g., Deng et al., 2019). A 30-m SRTM (Shuttle Radar Topography Mission)
169 DEM provided independent ground control points. Two (range) by two (az-
170 imuth) pixel multilooking was used to reduce speckle noise. The final DEMs
171 have a spatial resolution of 5×5 meters with a vertical precision of < 2 m.

172 **3.1.2 Terrestrial Radar**

173 We employed terrestrial radar interferometry (TRI) to assess the level of noise
174 in our topographic profiles (described below) from the 2017 TDX acquisition.
175 Although this comparison does not give us a direct assessment of noise for the
176 2012 DEM (the model from which we are measuring channel incision depths),
177 it gives a relative level of confidence in our TDX DEM processing methods.
178 TRI is a ground-based scanning radar that measures the amplitude and phase
179 of a backscattered microwave signal. A GAMMA real aperture radar operating
180 at Ku-band (1.74 cm wavelength) was used for this study. The TRI has one
181 transmitting antenna and two receiving antennas, which allows for topographic
182 mapping with a single scan (e.g. Dixon et al., 2012; Caduff et al., 2015; Voytenko
183 et al., 2015; Xie et al., 2018; Deng et al., 2019). The resolution of the range
184 measurements is ~ 1 m, and the azimuth resolution varies linearly with distance
185 (e.g., 1.8 m at 1 km distance, 7 m at 4 km). The spatial coverage of TRI is much
186 smaller compared to satellite imaging. Details of TRI data processing for DEM
187 generation are given in Strozzi et al. (2012) and Xie et al. (2018). TRI surveys
188 were conducted in December 2015 and April 2016. We use results from the
189 2016 campaign because it occurred towards the end of the eruption period and
190 is temporally closer to the 2017 TDX acquisition. The TRI DEM has a 5×5 m
191 resolution with an accuracy < 5 m and covers the incised portion of the channel
192 (Fig. 5).

193 **3.2 Channel Profiles and Depth Calculation**

194 Previous GIS-based methods used to determine paleotopography of volcanic
195 terrains (e.g., Germa et al., 2015) interpolate missing topography based on
196 connecting high points in elevation. Studies of fluvial channel erosion in steep
197 terrain generally do not deal with incision into conical edifices (Robl et al., 2008;

198 Fox, 2019). Additionally, these approaches model down-section and not cross-
199 section morphology, which we require to accurately measure incision depth and
200 extract cross-section profiles. We developed an elliptical least-square best-fit
201 contour method to obtain incision depths along the channel on Momotombo's
202 steep slopes to fill this application gap. We use this method to obtain channel
203 depths and cross-channel profiles from the 2012 and 2017 TDX DEMs and the
204 2016 TRI DEM. Our depth measurements are minimum values, as it is likely
205 that the eroding flow would have emplaced some volume of lava within the
206 channel. We also use this method to determine if any incision occurred during
207 the 2015 lava flow. Additionally, comparing the post-2015 TDX and TRI DEMs
208 provides an indication of noise within our channel measurements.

209 This approach measures incision depth against modeled paleotopography
210 created from optimized elliptical contours. A path down the channel's center
211 was defined with a sampling density set to the resolution of the DEM (5 m
212 for this study)(Fig. S1a). The widths of the channel and levees, determined
213 visually, were masked out in order to separate their signal from the overall signal
214 of the cone. A refined elliptical fit for the uppermost contour of the channel path
215 was calculated by minimizing the mean-squared difference between the actual
216 elevation contour and an elliptical contour. This optimized ellipse was then used
217 to calculate a fit to the elevation contour below. This second recalculated ellipse
218 was then fit to the next elevation contour, and so forth, until the end of the
219 designated channel path was reached. The output of this process is a modeled
220 paleotopography with no channel or levee structures (Fig. S1b). The incision
221 depth was calculated against the modeled paleotopography. The normal vector
222 to the paleotopographic model was calculated at each point, spaced 5 m apart
223 along each elliptical contour. As before, the normal vector was calculated by
224 fitting a plane to 8 adjacent points (three from the contour above, three from

225 the contour below, and two adjacent points from the same contour) (Fig. S1c).
226 The DEM was then re-orientated such that the z-axis was coincident with the
227 calculated normal vector. The incision depth was returned as a weighted average
228 of the constituent points, with weighting criteria based on the distance of the
229 points to the center of the plane (i.e., the point closest to the center had the
230 greatest weight) (Fig. S1d). This process was repeated for each point along the
231 contour, and then for every contour. This process allowed us to measure the
232 incision depth throughout the channel while removing the conic signal of the
233 edifice (Fig. 6). Incision depth varied from 35 m at the summit rim and tapers
234 off to 0 at ~ 600 m elevation (Fig. 7). We calculate the eroded volume of the
235 channel to be $4 \times 10^5 \text{ m}^3$. A profile of each cross-channel contour was calculated
236 for the 2012 and 2017 TDX and 2016 TRI DEMs (Fig. 8).

237 Results show the pre-2015 eruption channel extended down the northeast
238 side of the edifice from the summit and incised into the summit (Fig. 6). The
239 2015 lava flow follows the same path as the pre-eruption channel (Fig 8). The
240 elliptical contour fit method was also applied to the 2016 TRI DEM. Data gaps
241 within the DEM were filled using a regularized spline with tension interpolation
242 method in QGIS and the same process described above was utilized. We provide
243 the code for this method (S1) and an additional code for a circular fit method
244 in the Supplemental Documentation (S2).

245 **4 Discussion**

246 **4.1 Channel Origins**

247 The difference between modeled paleotopography and the 2012 TDX DEM
248 shows that a channel has cut into the edifice. The distribution of lava flows
249 beneath the 1905 units, shown in Figure 1, implies that no structure existed in

250 this location prior to 1905 to consistently direct the path of subsequent lava flows
251 (as was the case for the 2015 eruption). No historical reports note a leveed lava
252 channel on the NE flank of Momotombo prior to the 1905 eruption (Vincent,
253 1890; Intercontinental Railway Commission, 1898; Sapper, 1925). Examination
254 of the area surrounding Momotombo shows no down-slope deposition of suffi-
255 cient volume to support a channel having carved into the NE edifice prior to the
256 1905 eruption by environmental erosion (e.g. hydrologic erosion) and then in-
257 filled by subsequent lava flows. The rest of the edifice is similarly devoid of any
258 large-scale drainage features (e.g. barrancas, rilles, or gullies). DEM analyses
259 show the channel width is uniform from summit to low on the slopes (Fig. 2a).
260 Incised channels on other volcanoes (e.g., Merapi, Nevado del Ruiz) are gener-
261 ally much wider at the mouth, less consistent in width, and are less linear than
262 Momotombo's channel because they are related to more violent hazards (e.g.,
263 pyroclastic density currents and lahars). Results also show it was unlikely that
264 erosion occurred during the 2015 lava flow, given that it flowed over the armored
265 channel and not a variably consolidated slope of cinders and spatter/agglutinate
266 (Fig. 7). In the absence of evidence that suggests otherwise, we conclude that
267 channel most likely formed during the emplacement of the 1905 lava flow.

268 **4.1.1 Thermal Erosion**

269 The total energy emitted by the 1905 lava flow, calculated using Equation 1,
270 is about 7×10^{16} J for an eruptive volume of 2×10^7 m³. Taking into account
271 the energy balance between heat sources (85% retained) and sinks (15% lost)
272 described in Wooster et al. (1997), we calculate that 6×10^{16} J is the minimum
273 amount of the original energy that remained within the flow. Although the
274 length of time used to calculate this ratio for the Mount Etna eruption was
275 greater than the duration of the Momotombo eruption, it is helpful to place a
276 first order constraint on how much thermal energy is lost into the environment.

277 We calculate the total energy needed to fully erode the channel is about 2
278 $\times 10^{14}$ J, by substituting the mass of the eroded section of the channel into
279 Equation 1. Although we find that sufficient energy exists within the system
280 to erode the substrate, we note that not all of the energy present is available
281 for this purpose. Had all of this energy been used to erode, the thermal loss
282 would have been sufficiently great that the emplaced flow would be much thicker
283 and shorter than what is observed. Modeling the depth of heat transfer into
284 the substrate as a function of time using Equation 2 estimates the growth of
285 the substrate thermal boundary layer at 8.8 cm per day. Thermal erosion rates
286 in Hawaiian tubes and channels can reach ~ 10 cm per day (Kauahikaua et al.,
287 1998); given the lower temperature of lavas erupted on Momotombo, a slower
288 rate of thermal boundary layer growth makes sense. Given the short duration of
289 the 1905 eruption (< 1 week; Sapper, 1925), thermal erosion by itself is unlikely
290 to have formed the observed morphology.

291 **4.1.2 Thermo-mechanical Erosion**

292 Conceptually, once the near-subsurface reaches the threshold temperature, which
293 we assert is the glass transition (1013 K, Giordano et al., 2005), the hotter sub-
294 surface material is transported downhill by the lava flow. For this assumption
295 to be correct, the slope has to be steep and the lava flow velocity at its base has
296 to be fast. This implies that the thermal boundary layer reaches some critical
297 thickness and is then eroded away mechanically by the lava flow. While this
298 process surely contributes to incision of the channel, it cannot fully account for
299 the observed depths. It is possible H varies with distance along the channel
300 because the underlying substrate changes from very soft material at the top of
301 the cone to harder material lower on the flanks. We reject this because the sur-
302 face of the edifice is a relatively uniform slope without major lithologic changes.
303 These results provide insight into how heat is transferred into the substrate over

304 time, which helps us understand how the material hardness of the substrate, H ,
305 is reduced over time as the lava flow moves downslope.

306 We assume that the growth and removal of the thermal boundary layer over
307 time can be approximated as a steady state process, captured by the depth
308 of incision at each point along the channel. An exponential was fit to the
309 incision depth data to extract the quadratic function of $d_{channel}$ in terms of
310 incision depth and elevation (Fig. 10). We solve for H and find that the lowest
311 value (corresponding to softest substrate) was 4.8×10^5 Pa corresponding to
312 an incision depth of 30 m (Fig. 10). These results show the hardness of the
313 substrate increases as a function of time, but note that we use depth as proxy
314 for time. Realistically, the deepest incision points are closest to the vent because
315 they have been exposed to erosive work for a greater amount of time. The
316 function modeled to from Equation 3 tackles that problem from the opposite
317 perspective (i.e., it models the decrease in erosive depth, which suggests increase
318 in hardness). We know that temperature is increasing in the substrate based on
319 the relationships described in Equation 2, which decreases the hardness, so we
320 revise these results and report them as a decrease in hardness over time to more
321 accurately reflect the physical processes controlling the incision depth. Detailed
322 historical observations list the eruption duration as six to seven days in length,
323 which allows us to place constraints on the rate of change of hardness (Fig. 9)
324 (Sapper, 1925).

325 4.2 Channel Growth

326 We calculate that the eroded volume is equal to roughly 2% of the total volume
327 of the 1905 lava flow. Given the low eruptive temperature of basaltic andesites, it
328 is unlikely that this material was fully assimilated into the flow. As the material
329 heats and softens it is likely dragged downslope along the base of the flow for

330 a short distance and then re-deposits, which creates a scalloped type signal for
331 the measure of incision depth against elevation (Fig. 7). The thicknesses of
332 subsequent lava flows will respond to this subtle topographic variability (i.e.,
333 more lava will be deposited in the troughs, less on the crest), which we find to
334 be true for the 2015 flow (Fig. 7). We also note a strong correlation between
335 incision and lack of developed levees in the 2012 TDX DEM, which suggests that
336 erosion began early on during the eruption (Fig. 8, conceptualized in Fig. 12).
337 This implies that levee bounded incised channels are not thermo-mechanically
338 eroded, which is an important consideration for studies of incised channels on
339 other planetary bodies.

340 **4.3 Morphologic Implications**

341 The depth of a thermally eroded channel is limited by the efficiency of heat
342 transfer across the boundary between the lava flow and the substrate, the rate
343 of heat transfer in the subsurface, and the duration of an eruption (Kerr, 2001);
344 when combined with morphologic studies of emplacement conditions (especially
345 time), a constraint can be placed on the maximum depth of erosion. Channels
346 whose incision depth exceeds this threshold indicate a preferential hardness
347 ratio of the substrate to the flow (i.e., it is softer than the overriding flow) and
348 can therefore be used to determine the presence of pyroclastic rocks and other
349 easily eroded terrain (e.g., unconsolidated regolith, alluvial deposits, etc.) on
350 planetary surfaces that can only be observed remotely. Large flows on the Moon,
351 in particular, may be worth revisiting in light of these findings (Hurwitz et al.,
352 2013).

353 A 1528 drawing of Momotombo by Oviedo (Fernandez de Oviedo y Valdes,
354 1528) shows a similar channel on the volcano's west side. A channel on the
355 northern flank (likely emplaced during an eruption in the second half of the

1800's Sapper (1925)) is also incised into the cone, and has been infilled by cin-
ders from subsequent eruptions, which suggests the processes of slope incision
and subsequent infill occurs with relative frequency on Momotombo. The pref-
erential diversion of lava flows into incised channels for future events suggest
that lava flow hazards on some steep-sided volcanoes are influenced by the cre-
ation, infill, and eventual abandonment of these structures. The channel may
limit the lava flow hazard for the western flank if the next eruption is similar in
size. Understanding the evolution of these features has important implications
for lava flow hazards and growth patterns and erosion of composite volcanoes.

5 Conclusions

We use satellite (TDX) and terrestrial radar (TRI) DEMs to obtain a detailed
record of recent changes to the edifice of Momotombo Volcano from 2012–2017,
during which a VEI-2 eruption occurred. We describe a unique lava channel
that incised 25–35 m into the northeast sector of the volcano near the summit
and transitions into a constructional channel roughly halfway down the edifice.
We assert that this feature formed erosively during the emplacement of a lava
flow in 1905 and note a direct correlation between a lack of levees and incision
depth. Thermal erosion alone was unable to account for the full depth of incision
and we suggest that thermo-mechanical erosion is the likely cause. We examine
inputs from mechanical models of erosion and determine that, based on the
relationship between material hardness and shear strength, these models should
be re-classified as thermo-mechanical. We propose that the transfer of heat into
the substrate decreases the hardness of the material, which encourages it to
flow more readily and excavate. We establish that the critical temperature at
which this occurs is lower than previously thought, likely at the glass transition
temperature (1013K), instead of the liquidus of a given lava. We calculate the

382 total eroded volume to be $4 \times 10^5 \text{ m}^3$ and determine a minimum hardness of 4.8
383 $\times 10^5 \text{ Pa}$ at the deepest point of incision for the 1905 eruption. Deeply incised
384 channels control the distribution of future flows and can also be used to infer
385 the material properties of the substrate into which they are excavated.

386 **Acknowledgments**

387 Funding for field work was provided by NSF EAR 1620977: Geochemical and
388 Geophysical Observations of the 2015 Eruption of Volcan Momotombo, Nicaragua,
389 awarded to PL, CC, and others. Field support was provided by many staff at
390 INETER. Equipment logistics were eased by the efforts of Denis Voytenko and
391 Milton Ordonez. The manuscript's clarity was improved by feedback from Jen
392 Bright, facilitated by Pam Wayne and Jose Rincon.

393 References

- 394 Baker, V. R., Komatsu, G., Parker, T. J., Gulick, V. C., Kargel, J. S., and
395 Lewis, J. S. (1992). Channels and valleys on Venus: Preliminary analysis of
396 Magellan data. *Journal of Geophysical Research. Planets*, 97(E8):13421.
- 397 Beresford, S., Cas, R., Lahaye, Y., and Jane, M. (2002). Facies architecture of an
398 archean komatiite-hosted ni-sulphide ore deposit, victor, kambalda, western
399 australia: implications for komatiite lava emplacement. *Journal of Volcanol-
400 ogy and Geothermal Research*, 118(1):57 – 75.
- 401 Bilotta, G., Cappello, A. and Herault, A., and Del Negro, C. (2019). Influ-
402 ence of topographic data uncertainties and model resolution on the numerical
403 simulation of lava flows. *Environmental Modelling and Software*, 112:1–15.
- 404 Caduff, R., Schlunegger, F., Kos, A., and Wiesmann, A. (2015). A review of ter-
405 restrial radar interferometry for measuring surface change in the geosciences.
406 *Earth Surface Processes and Landforms*, (2):208.
- 407 Carr, M. J. and Pontier, N. K. (1981). Research paper: Evolution of a young
408 parasitic cone towards a mature central vent; Izalco and Santa Ana volcanoes
409 in El Salvador, Central America. *Journal of Volcanology and Geothermal
410 Research*, 11:277 – 292.
- 411 Courtland, L. M., Kruse, S. E., Connor, C. B., Connor, L. J., Savov, I. P.,
412 and Martin, K. T. (2012). Gpr investigation of tephra fallout, cerro negro
413 volcano, nicaragua: a method for constraining parameters used in tephra
414 sedimentation models. *Bulletin of Volcanology*, (6):1409.

- 415 Deng, F., Rodgers, M., Xie, S., Dixon, T. H., Charbonnier, S., Gallant, E. A.,
416 Vlez, C. M. L., Ordoez, M., Malservisi, R., Voss, N. K., and Richardson,
417 J. A. (2019). High-resolution dem generation from spaceborne and terrestrial
418 remote sensing data for improved volcano hazard assessment a case study at
419 nevado del ruiz, colombia. *Remote Sensing of Environment*, 233:111348.
- 420 Dietterich, H., Lev, E., Chen, J., Richardson, J., and Cashman, K. (2017).
421 Benchmarking computational fluid dynamics models of lava flow simulation
422 for hazard assessment, forecasting, and risk management. *Journal of Applied*
423 *Volcanology*, 6(1):1.
- 424 Dietterich, H. R. and Cashman, K. V. (2014). Channel networks within lava
425 flows: Formation, evolution, and implications for flow behavior. *Journal of*
426 *Geophysical Research. Earth Surface*, 119(8):1704.
- 427 Dixon, T. H., Voytenko, D., Lembke, C., Pea, S., Howat, I., Gourmelen, N.,
428 Werner, C., and Oddsson, B. (2012). Emerging technology monitors ice-sea
429 interface at outlet glaciers. *Eos (0096-3941)*, 93(48):497.
- 430 Dundas, C. M. and Keszthelyi, L. P. (2014). Emplacement and erosive effects
431 of lava in south Kasei Valles, Mars. *Journal of Volcanology and Geothermal*
432 *Research*, 282:92 – 102.
- 433 Fagents, S. A. and Greeley, R. (2001). Factors influencing lava-substrate heat
434 transfer and implications for thermomechanical erosion. *Bulletin of Volcanol-*
435 *ogy*, (8):519.
- 436 Fernandez de Oviedo y Valdes, G. (1528). Infierno de mamea.
- 437 Fox, M. (2019). A linear inverse method to reconstruct paleo-topography. *Ge-*
438 *omorphology*, 337:151 – 164.

- 439 Germa, A., Lahitte, P., and Quidelleur, X. (2015). Construction and destruc-
440 tion of Mont Pele volcano: Volumes and rates constrained from a geomorpho-
441 logical model of evolution. *Journal of Geophysical Research. Earth Surface*,
442 120(7):1206.
- 443 Giordano, D., Nichols, A. R., and Dingwell, D. B. (2005). Glass transition
444 temperatures of natural hydrous melts: a relationship with shear viscosity
445 and implications for the welding process. *JOURNAL OF VOLCANOLOGY*
446 *AND GEOTHERMAL RESEARCH*, (1-2):105.
- 447 Global Volcanism Program (2017). Report on Momotombo (Nicaragua). In Ven-
448 zke, E., editor, *Bulletin of the Global Volcanism Network*, volume 42:1, Smith-
449 sonian Institution. <https://doi.org/10.5479/si.GVP.BGVN201701-344090>.
- 450 Gottsmann, J. and Dingwell, D. B. (2002). The thermal history of a spatter-fed
451 lava flow: the 8-ka pantellerite flow of mayor island, new zealand. *Bulletin of*
452 *Volcanology*, 64(6):410–422.
- 453 Greeley, R., Fagents, S. A., Scott Harris, R., Kadel, S. D., Williams, D. A.,
454 and Guest, J. E. (1998). Erosion by flowing lava: Field evidence. *Journal of*
455 *Geophysical Research*, (B11):27.
- 456 Head, J. W. and Wilson, L. (2017). Generation, ascent and eruption of magma
457 on the Moon: New insights into source depths, magma supply, intrusions
458 and effusive/explosive eruptions (Part 2: Predicted emplacement processes
459 and observations). *Icarus*, 283(Lunar Reconnaissance Orbiter - Part II):176
460 – 223.
- 461 Hill, B. E., Connor, C. B., Jarzempa, M. S., La Femina, P. C., Navarro, M., and
462 Strauch, W. (1998). 1995 eruptions of cerro negro volcano, nicaragua, and
463 risk assessment for future eruptions. *Geological Society of America Bulletin*,
464 (10):1231.

- 465 Hobden, B. J., Houghton, B. F., and Nairn, I. A. (2002). Growth of a young,
466 frequently active composite cone: Ngauruhoe volcano, New Zealand. *Bulletin*
467 *of Volcanology*, (6):392.
- 468 Hurwitz, D. M., Fassett, C. I., Head, J. W., and Wilson, L. (2010). Formation
469 of an eroded lava channel within an Elysium Planitia impact crater: Dis-
470 tinguishing between a mechanical and thermal origin. *Icarus*, 210(2):626 –
471 634.
- 472 Hurwitz, D. M., Head, J. W., and Hiesinger, H. (2013). Lunar sinuous rilles:
473 Distribution, characteristics, and implications for their origin. *Planetary and*
474 *Space Science*, 79-80:1–38.
- 475 Intercontinental Railway Commission (1898). A Condensed Report of the Trans-
476 actions of the Commission and of the Surverys and Explorations of its Engi-
477 neers in Central and South America.
- 478 Kauahikaua, J., Cashman, K. V., Mattox, T. N., Heliker, C. C., Hon, K. A.,
479 Mangan, M. T., and Thornber, C. R. (1998). Observations on basaltic lava
480 streams in tubes from Kilauea Volcano, island of Hawai'i. *Journal of Geophys-*
481 *ical Research. Solid Earth*, 103(B11):27303.
- 482 Kerr, R. C. (2001). Thermal erosion by laminar lava flows. *Journal of Geophys-*
483 *ical Research*, (11):26.
- 484 Kerr, R. C., Griffiths, R. W., and Cashman, K. V. (2006). Formation of chan-
485 nelized lava flows on an unconfined slope. *Journal of Geophysical Research:*
486 *Solid Earth (1978-2012)*, 111(B10).
- 487 Kilburn, C. R. J. and Lopes, R. M. C. (1988). The growth of AA lava flow
488 fields on Mount Etna, Sicily. *Journal of Geophysical Research: Solid Earth*,
489 93(B12):14759–14772.

490 Kirainov, V., Melekestev, I., Ovsyannikov, A., and Andreev, V. (1988). Re-
491 construction of the eruptive activity of momotombo volcano (nicaragua) to
492 assess volcanic hazards. pages 495 – 498.

493 Krieger, G., Moreira, A., Fiedler, H., Hajnsek, I., Werner, M., Younis, M.,
494 and Zink, M. (2007). TanDEM-X: A Satellite Formation for High-Resolution
495 SAR Interferometry. *IEEE Transactions on Geoscience and Remote Sensing*,
496 (11):3317.

497 Miller, A. A. (1963). Free volume and viscosity of liquids: Effects of temperature.
498 *The Journal of Physical Chemistry*, 67(5):1031–1035.

499 Patrick, M. R., Dehn, J., and Dean, K. (2004). Numerical modeling of lava
500 flow cooling applied to the 1997 okmok eruption: Approach and analysis (doi
501 10.1029/2003jb002537). *JOURNAL OF GEOPHYSICAL RESEARCH -ALL*
502 *SERIES-*, (3):B03202.

503 Peterson, D. W., Holcomb, R. T., Tilling, R. I., and Christiansen, R. L. (1994).
504 Development of lava tubes in the light of observations at Mauna Ulu, Kilauea
505 Volcano, Hawaii. *Bulletin of Volcanology*, (5):343.

506 Richardson, P. and Karlstrom, L. (2019). The multi-scale influence of topogra-
507 phy on lava flow morphology. *Bulletin of Volcanology*, (4):1.

508 Robl, J., Stwe, K., and Hergarten, S. (2008). Channel profiles around himalayan
509 river anticlines: Constraints on their formation from digital elevation model
510 analysis. *Tectonics*, 27(3).

511 Sapper, K. (1925). *Los volcanes de la America Central*. Halle: Verlag von Max
512 Niemeyer.

513 Schenk, P. M. and Williams, D. A. (2004). A potential thermal erosion lava
514 channel on Io. *Geophysical Research Letters*, 31(23).

- 515 Siewert, J. and Ferlito, C. (2008). Mechanical erosion by flowing lava. *Contem-*
516 *porary Physics*, (1):43.
- 517 Sklar, L. and Dietrich, W. E. (1998). River Longitudinal Profiles and Bedrock
518 Incision Models: Stream Power and the Influence of Sediment Supply. *Geo-*
519 *physical Monograph - American Geophysical Union*, page 237.
- 520 Staude, S., Barnes, S. J., and Le Vaillant, M. (2017). Thermomechanical ero-
521 sion of ore-hosting embayments beneath komatiite lava channels: Textural
522 evidence from kambalda, western australia. *Ore Geology Reviews*, 90:446 –
523 464.
- 524 Strozzi, T., Werner, C., Wiesmann, A., and Wegmuller, U. (2012). Topogra-
525 phy Mapping With a Portable Real-Aperture Radar Interferometer. *IEEE*
526 *Geoscience and Remote Sensing Letters*, (2):277.
- 527 Turcotte, D. L., Turcotte, D. L., and Schubert, G. (2002). *Geodynamics*. Cam-
528 bridge ; New York : Cambridge University Press.
- 529 Vincent, F. (1890). In and out of Central America.
- 530 Voytenko, D., Dixon, T. H., Luther, M. E., Lembke, C., Howat, I. M., and de la
531 Pea, S. (2015). Observations of inertial currents in a lagoon in southeastern
532 Iceland using terrestrial radar interferometry and automated iceberg tracking.
533 *Computers and Geosciences*, 82:23 – 30.
- 534 Williams, D. A., Kerr, R. C., and Lesher, C. M. (1998). Emplacement and
535 erosion by archean komatiite lava flows at kambalda: Revisited. *Journal of*
536 *Geophysical Research*, (B11):27.
- 537 Williams-Jones, G., Williams-Jones, A. E., and Stix, J. (1998). The nature
538 and origin of Venusian canali. *Journal of Geophysical Research. Planets*,
539 103(E4):8545.

- 540 Wilson, L. and Head, J. W. (2017). Generation, ascent and eruption of magma
541 on the Moon: New insights into source depths, magma supply, intrusions and
542 effusive/explosive eruptions (Part 1: Theory). *Icarus*, 283(Lunar Reconnaissance
543 sance Orbiter - Part II):146 – 175.
- 544 Wooster, M. J., Wright, R., Blake, S., and Rothery, D. A. (1997). Cooling
545 mechanisms and an approximate thermal budget for the 1991-1993 Mount
546 Etna lava flow. *Geophysical Research Letters*, (24):3277.
- 547 Xie, S., Dixon, T. H., Voytenko, D., Fanghui, D., and Holland, D. M.
548 (2018). Grounding line migration through the calving season at Jakobshavn
549 Isbr, Greenland, observed with terrestrial radar interferometry. *Cryosphere*,
550 12(4):1387 – 1400.

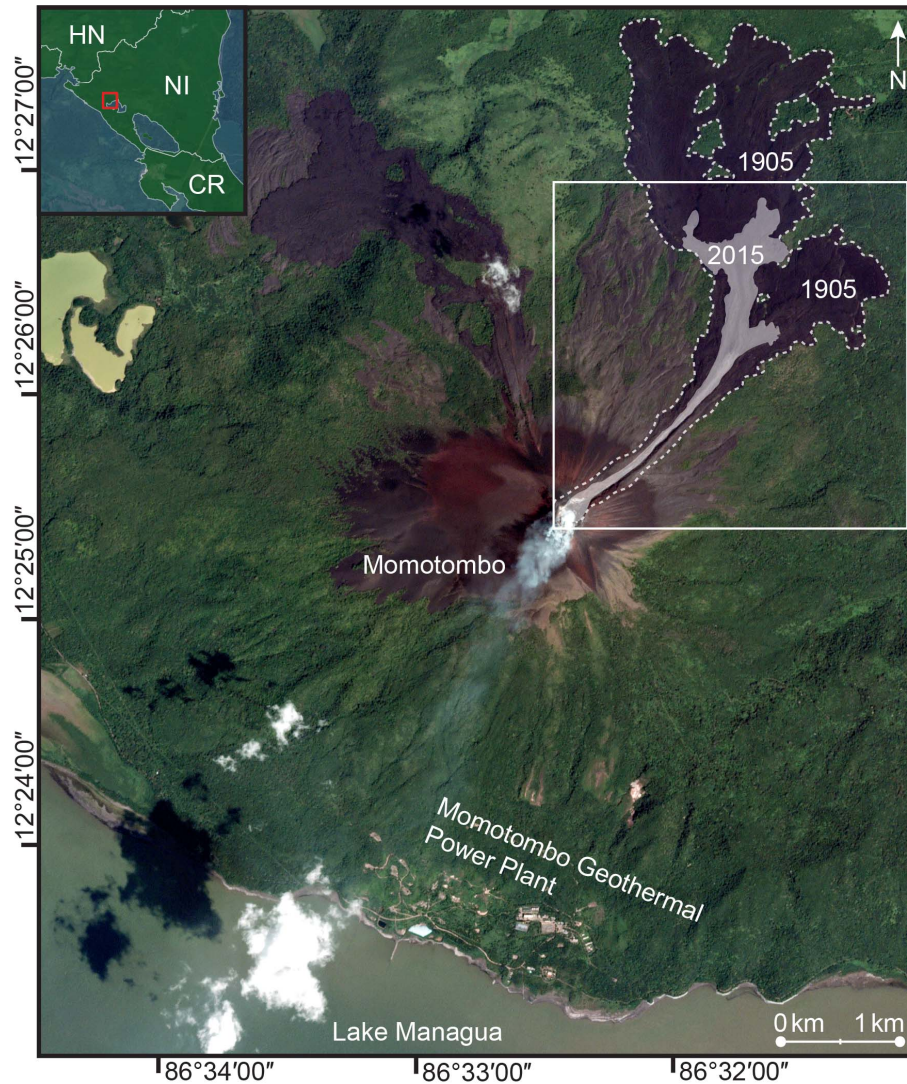


Figure 1: Momotombo area map. The most recent volcanism (a lava flow emitted during the 2015-2016 eruption) is noted by a light-grey overlay. The 1905 eruption is noted by a dotted line. The area shown in Fig. 4 is noted by the white box. Note the widely dispersed flows that underlie the 2015 and 1905 flows. Their distribution suggests that no incised channel existed at the time of their emplacement to direct flow paths. Background image from GoogleEarth.

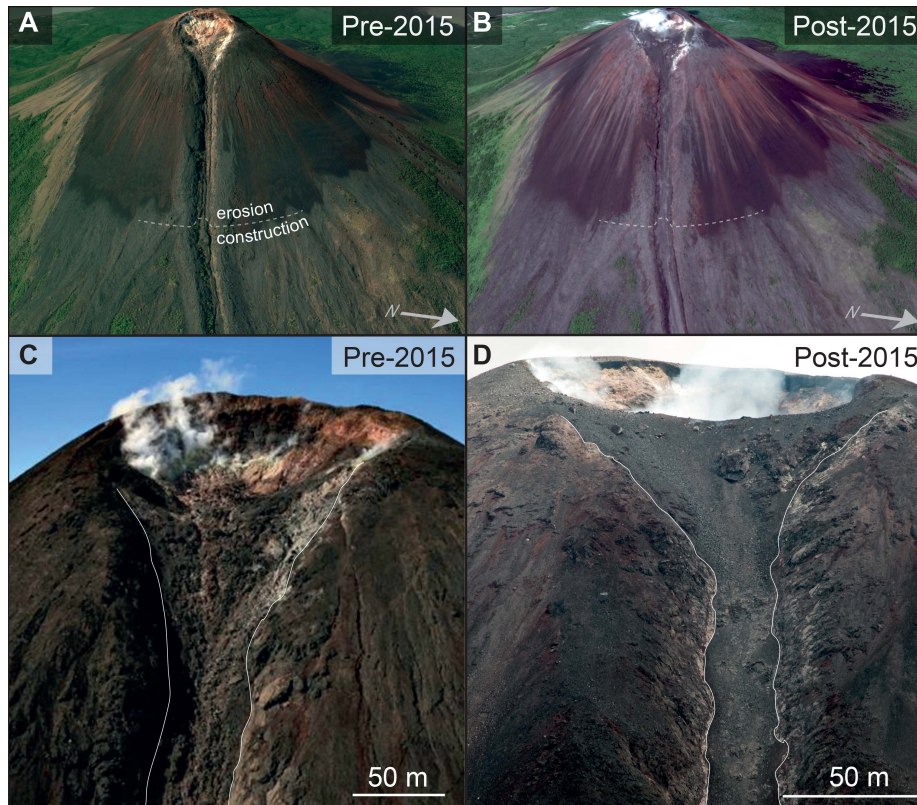


Figure 2: Pre and post 2015-2016 eruption images of the Momotombo channel and summit. A) A pre-eruption image of the channel, where the dashed line shows the approximate transition between erosional and constructional behavior. B) Major changes in morphology can be seen in and around the summit crater, where the 2015 lava flow first filled and was then partially excavated during subsequent explosions in 2016. The pre-existing floor of the channel has been paved over by a lava flow and appears less 'rough' than the pre-eruption channel floor. Images A and B from Google Earth. C) The summit crater prior to the 2015-2016 eruption, with white lines bounding the channel. Textures within the channel indicate downslope flow. Image from INETER. D) The summit area on 6 April, 2016. Several hundred small explosions have partially excavated a small dome from December, 2015. Blocks have been deposited atop the recent lava flow and a fine, grey layer of ash from repeated pyroclastic density currents coats the channel. Image from E. Gallant.

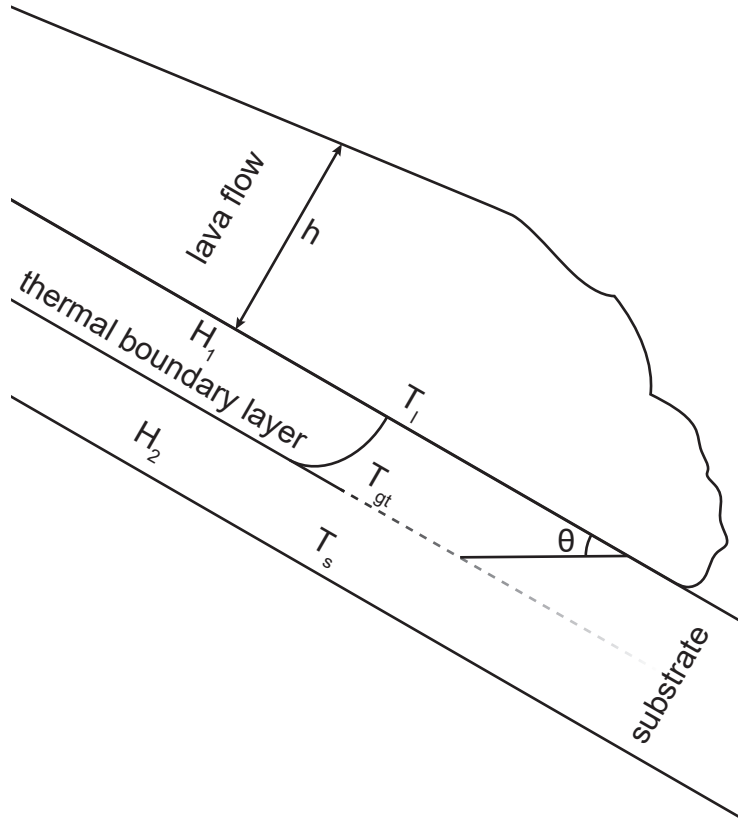


Figure 3: Thermal boundary formation illustration. The energy required to melt a pyroclast-rich substrate is less than that of a lava flow due to a lower density; we can therefore substitute the peak glass transition temperature (1013 K) as the minimum temperature required to initiate melting for such substrates (Giordano et al., 2005). The formation of the thermal boundary layer shows the transition between the temperature of the lava (T_l) and the substrate (T_s). This layer defines the boundary between a thermally softened substrate (H_1) and the unaffected substrate (H_2). The height of the lava flow is noted by h and the slope of the edifice by θ .

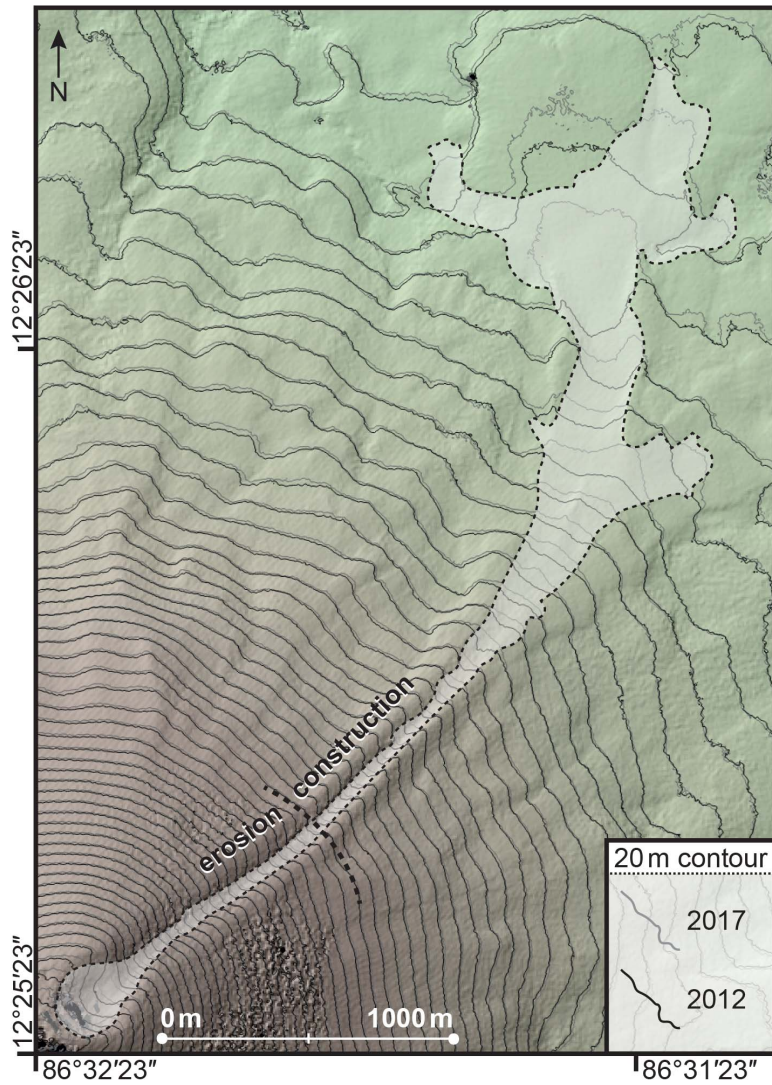


Figure 4: Elevation contour difference measured from the 2012 and 2017 TDX DEMs. Elevation contours at 20 m intervals were mapped from the TDX datasets; the grey contours represent the 2017 elevations (post 2015-2016 eruption), and the black represent the 2012 elevations. Slight contour variations exist in areas not impacted by the 2015-2016 eruption due to the different look angles of the TDX data pairs and georeferencing uncertainties. The dashed line and white infill show the area covered by the 2015 lava flow.

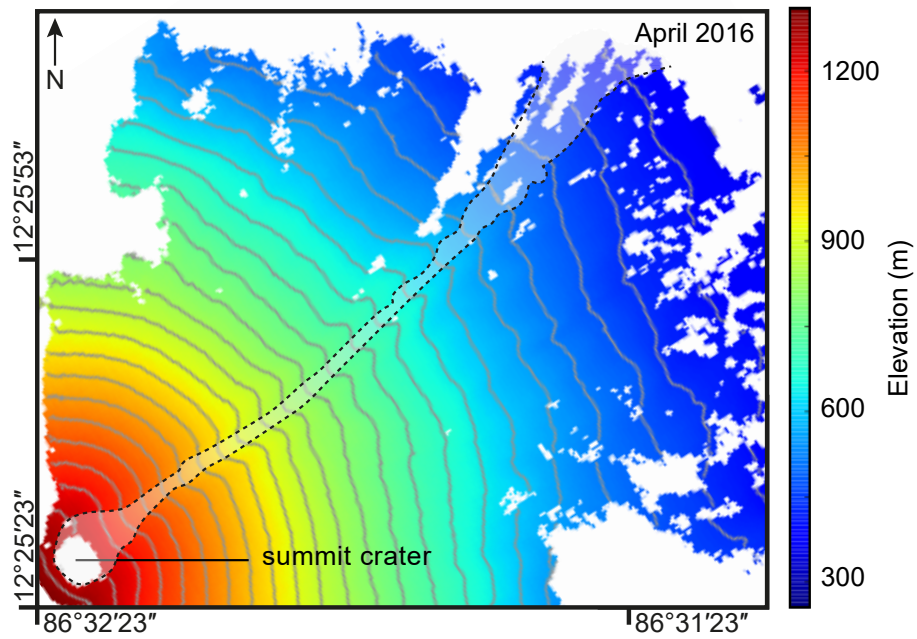


Figure 5: 2016 Terrestrial Radar DEM. The white infill and black dashed line shows the area covered by the 2015 lava flow. The absence of signal near the summit shows the 120×100 m crater, which was excavated by several hundred small explosions between December 2015 and April 2016. The grey lines indicate 20 m contour intervals.

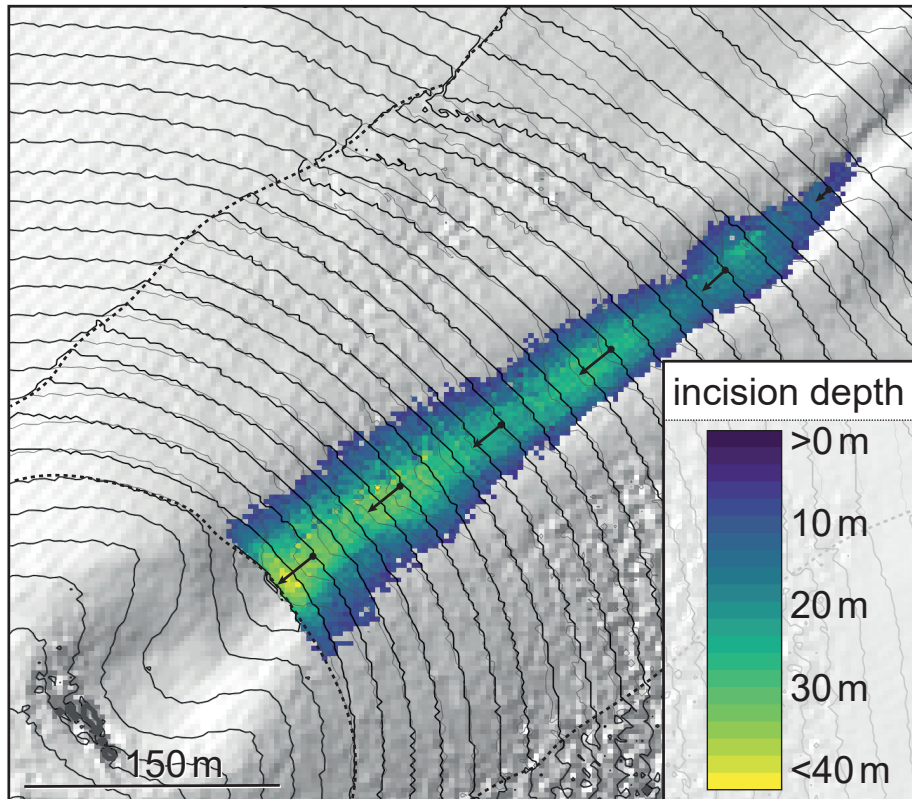


Figure 6: Elliptical contour fit incision depth process (from 2012 DEM). The original elevation contours at 20 m intervals are noted in grey, the modeled fit in black. Incision depths, with arrows that indicate the horizontal distance between the modeled paleotopography and the current point of corresponding incision. Incision is deepest at the summit and decreases downslope.

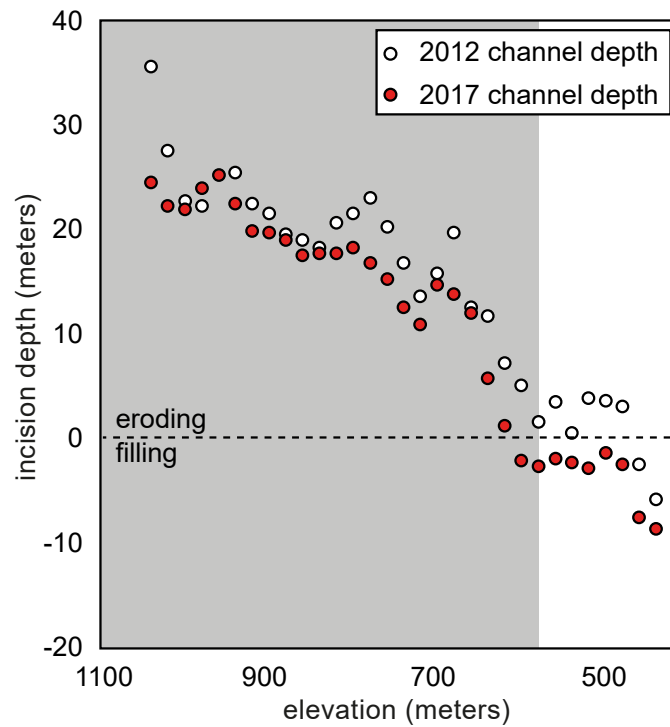


Figure 7: Calculated channel depths at 20-m elevation intervals before and after the eruption, using the elliptical fit method described in Figure 6. Calculated channel depths and slopes at 20-m elevation intervals before and after the eruption. White and red dots are channel depths of the pre- and post-eruption channel, respectively. The difference of the two DEMs gives us the thickness of the 2015 lava flow. The grey shading indicates the elevation range where erosion dominates (>650 m).

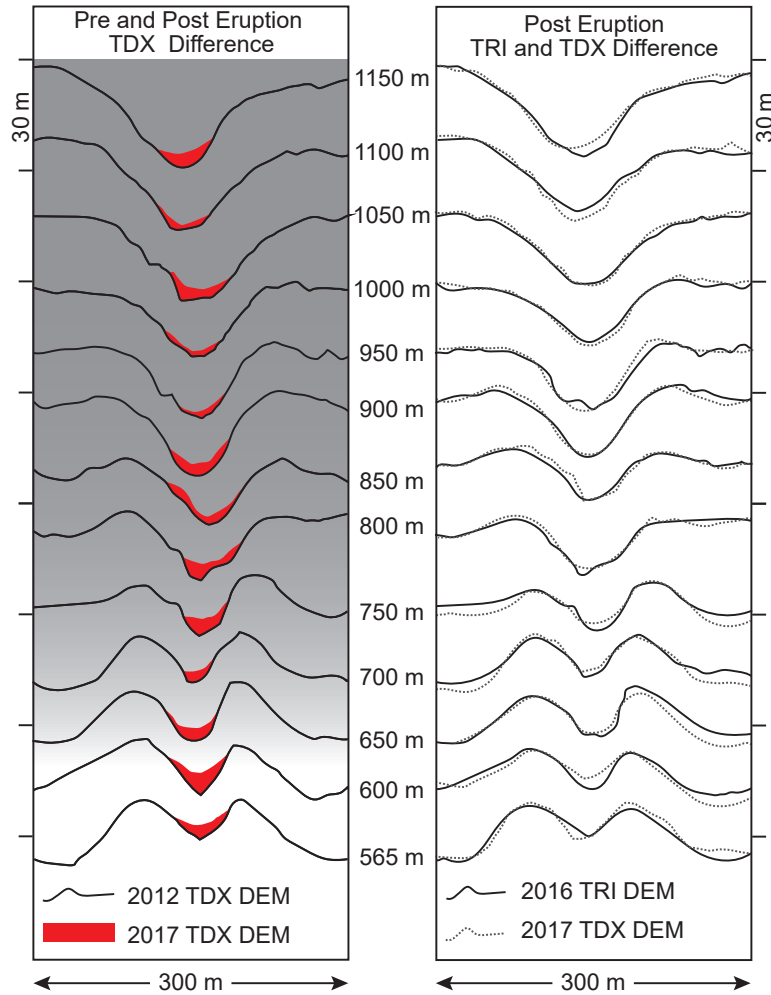


Figure 8: Momotombo lava channel profiles. The left figure shows channel profiles from the 2012 TDX DEM and an overlay of the lava flow from 2015. The 2012 profile is noted by the solid black line, with the 2015 lava flow (imaged by the 2017 TDX acquisition) by the red polygon. The grey shading illustrates the transition of channel into a constructional feature. The profiles have been visually adjusted to match up topography in order to account for the 21° difference in acquisition angles. The right figure shows the difference between the 2016 TRI DEM and the 2017 TDX DEM. Comparison of the post-eruption profiles estimates the relative noise of the DEMs.

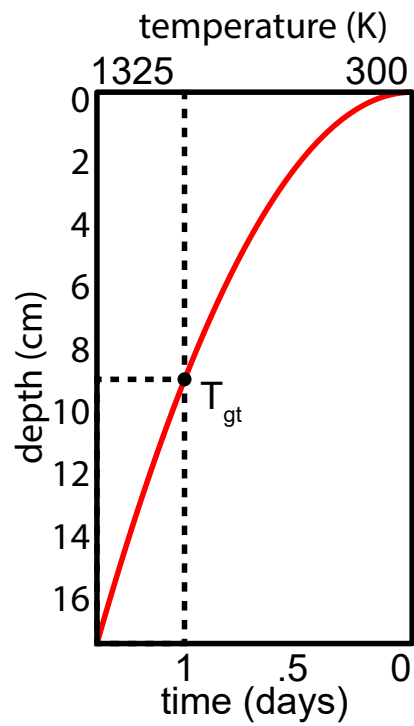


Figure 9: Substrate thermal boundary layer. At one day, we calculate the thermal boundary layer for a flow on Momotombo to grow to 8.8 cm. Thermal erosion rates in Hawaiian tubes and channels can reach ~ 10 cm per day (Kauahikaua et al., 1998); given the lower temperature of lavas erupted on Momotombo, it is reasonable to assume a slower rate of thermal boundary growth.

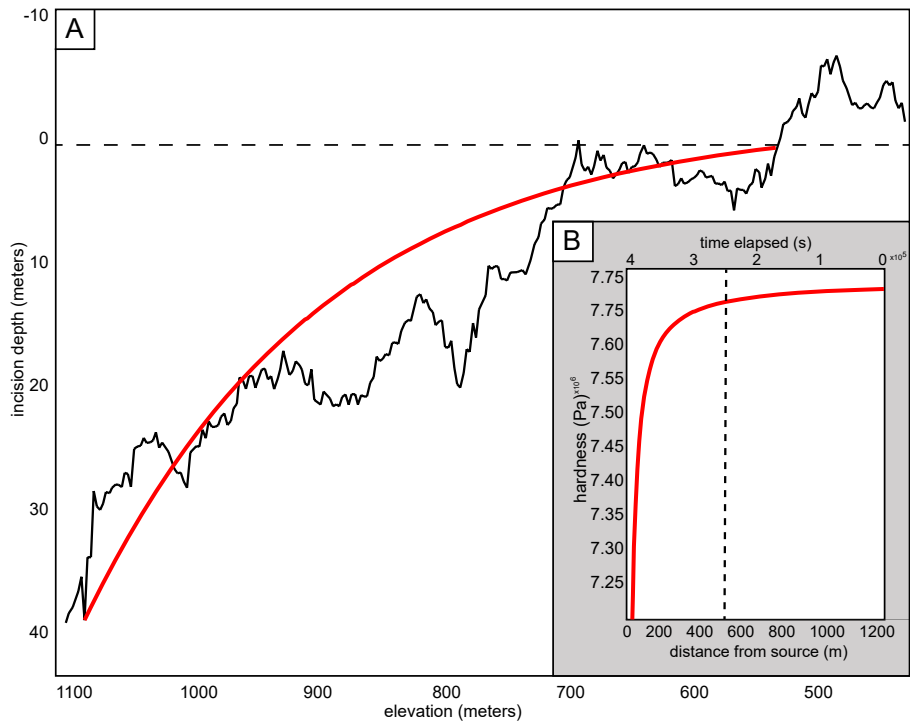


Figure 10: Incision depth fit models. A: Depth is used as a proxy for time in order to constrain the hardness (H) of the eroded substrate. The red line indicates the exponential fit to the eroded depth as a function of elevation. The dotted line indicates the the transition from erosion (below) to construction (above). B: Substrate hardness as a function of time and distance. The dotted line notes the transition from erosion (left) to construction (right). Time elapsed is the total time the substrate is in contact with flowing lava.

551 **Supplemental Material**

552 **Paleotopography Modeling Code**

553 The MatLab code and associated functions used to model the paleotopogra-
554 phy of the erosive channel and determine excavation depths is available at
555 https://github.com/elisabeth-gallant/USF_dissertation.

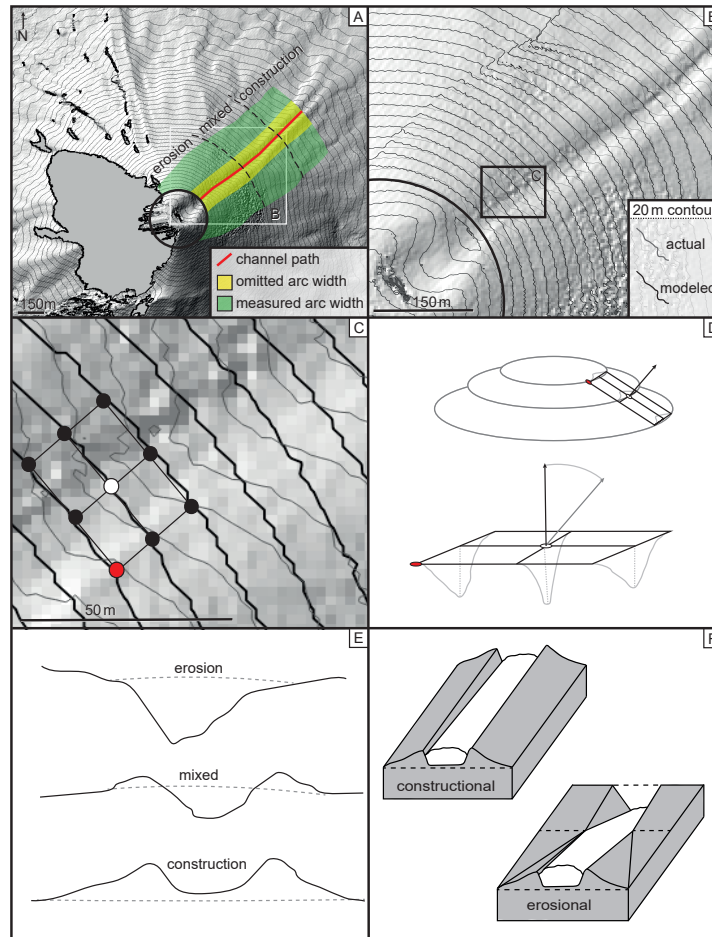


Figure 11: Elliptical contour fit incision depth process (from 2012 DEM). A: The center of the channel is noted in red, area used to calculate the best fit contours in green, and the area omitted from the contour calculation in yellow. The dashed line shows the approximate boundary between erosional, mixed, and constructional regimes (described in profile in panel F). B: The original elevation contours at 20 m intervals are noted in grey, the modeled fit in black. C: The orientation of vectors normal to the edifice are calculated using a 9×9 matrix. The distance between sampling points is enlarged to illustrate the concept. D: The matrix is transposed so that the only magnitude of the vector is in the z-direction. The elevation value is returned as a weighted-average of the constituent points (with distance from the center as the weighting criteria). E: The simplified profiles for erosional, mixed, and constructional regimes, with a dashed line denoting the paleosurface. F: Constructional (left) vs erosional (right) behaviour in lava channels on an incline. We note the change in slope associated with the original orientation of the incline and the eroded portion. The dashed line notes the paleotopography surface. Additionally, levees are absent from the incised section of the channel. Profiles of these different regimes are presented in Figure 8.

556 **Circular Contour Fit**

557 Channel incision depths were measured by interpolating best-fit 20-m interval
558 contour lines to the overall shape of the edifice using the 2012 TDX DEM. Each
559 interpolated contour line was calculated by fitting the original contour line with
560 an arc using least-squares. The section proximal to the channel was not included
561 in the fitting process due to its wide deviation from the overall shape of the cone.
562 Depth at each sampled elevation was measured by determining the minimum
563 distance between the interpolated contour line and the deepest point of the
564 channel, measured normal to the slope of the edifice (Fig. 12b). All points on
565 the contour line (not including the flow levees and the channel) were averaged
566 to calculate the slope for each measured depth.

567 Results show the pre-2015 eruption channel extended down the northeast
568 side of the edifice from the summit and continued for 2 km onto the surrounding
569 plain (Fig. 13). A consistent width of ~ 30 m was maintained throughout the
570 channels length, while incision depth varied from 35 m at the summits rim and
571 tapered off to 0 at ~ 700 m elevation (Fig. 12a). The 1905 channel has been
572 infilled with a lava flow from 2015 with a thickness < 3 m (Fig. 13).

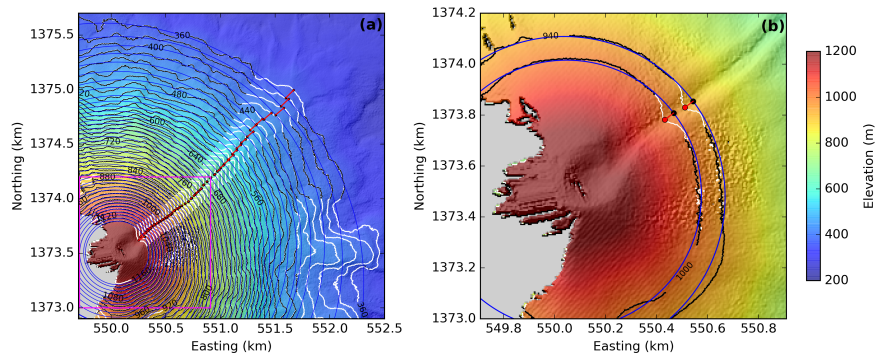


Figure 12: Channel depth calculation using the pre-eruption DEM as an example (a) 2012 DEM. Black and white lines are contours with 20 m interval. The blue circles are the best-fit arcs for each contour line. Contour lines in white were not used in the fitting processing because they include the topographic influence of the levees and channel, which greatly deviates from the circular fit. The red lines indicate the depth of the channel thalweg. (b) A zoomed in view of the fitting process. Red dots indicate the deepest points in the channel.

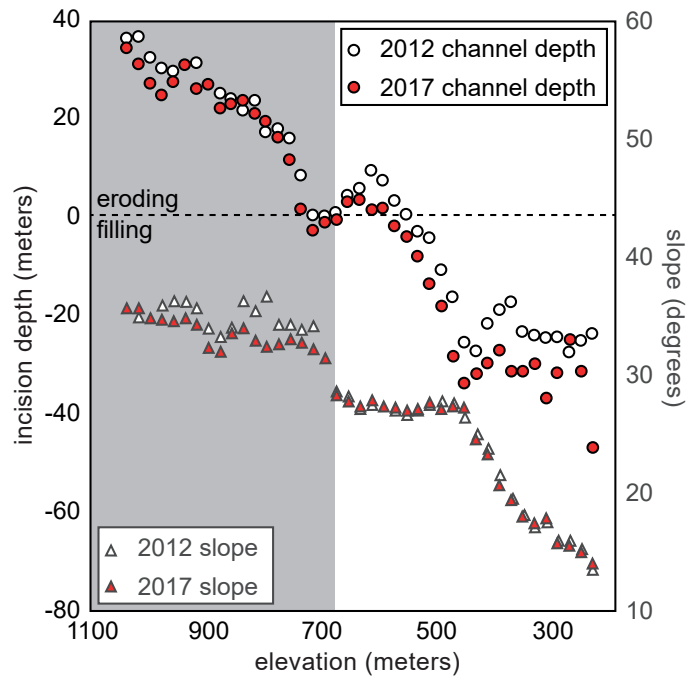


Figure 13: Calculated channel depths, slopes, and differences using the circular fit method. Calculated channel depths and slopes at 20-m elevation intervals before and after the eruption. White and red dots are channel depths of the pre- and post-eruption channel, respectively. The difference of the two DEMs gives us the thickness of the 2015 lava flow. White and red triangles are averaged slopes at 20-m elevation intervals of the pre- and post-eruption edifice.

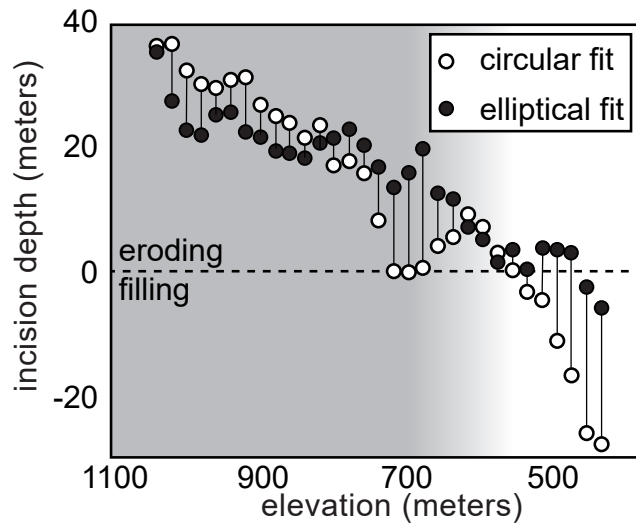


Figure 14: Comparison of the circular and elliptical method incision depths for the 2012 TDX DEM. The grey area indicates the transition between incision and construction, with a gradient to indicate the uncertainty between the two models as to where this occurs.